

Haptic bilateral teleoperation system for free-hand dental procedures

Lorenzo Pagliara, *Student Member, IEEE*, Enrico Ferrentino, *Member, IEEE*, Andrea Chiacchio, Giovanni Russo, *Senior Member, IEEE*

Abstract—Free-hand dental procedures are typically repetitive, time-consuming and require high precision and manual dexterity. Robots can play a key role in improving procedural accuracy and safety, enhancing patient comfort, and reducing operator workload. However, robotic solutions for free-hand procedures remain limited or completely lacking, and their acceptance is still low. To address this gap, we develop a haptic bilateral teleoperation system (HBTS) for free-hand dental procedures (FH-HBTS). The system includes a dedicated mechanical end-effector, compatible with standard clinical tools, and equipped with an endoscopic camera for improved visibility of the intervention site. By ensuring motion and force correspondence between the operator's actions and the robot's movements, monitored through visual feedback, we enhance the operator's sensory awareness and motor accuracy. Furthermore, recognizing the need to ensure procedural safety, we limit interaction forces by scaling the motion references provided to the admittance controller based solely on measured contact forces. This ensures effective force limitation in all contact states without requiring prior knowledge of the environment. The proposed FH-HBTS is validated in a dental scaling procedure using a dental phantom. The results show that the system improves the naturalness, safety, and accuracy of teleoperation, highlighting its potential to enhance free-hand dental procedures.

Index Terms—Haptics, teleoperation, interaction control, free-hand dental procedures, eye-hand coordination

I. INTRODUCTION

THE World Health Organization estimates that oral diseases affect nearly 3.5 billion people worldwide. However, access to primary oral health services is limited due to the high costs of procedures, the unequal distribution of oral health professionals, and the lack of adequate healthcare facilities [1].

Traditionally, routine, prosthetic, periodontal, and some surgical dental procedures are performed free-hand. Routine procedures include the treatment of dental caries and endodontic therapy, characterized by the mechanical excavation of the damaged or infected dental structure, typically utilizing burs attached to a rotary dental handpiece, followed by the replacement of the lost structure with a synthetic filling material [2]. Prosthetic procedures, on the other hand, focus on the replacement of missing or severely damaged teeth through the use of prostheses, such as inlays, crowns, or bridges.

This research was conducted in the frame of the Department of Excellence 2023/2027 Project

Lorenzo Pagliara, Enrico Ferrentino and Giovanni Russo are with the Department of Information Engineering, Electrical Engineering and Applied Mathematics (DIEM), University of Salerno, 84084 Fisciano, Italy, e-mail: {lpagliara, eferrentino, giovarusso}@unisa.it

Andrea Chiacchio is with the Specialization School in Oral Surgery, University of Naples Federico II, 80138 Napoli, Italy, e-mail: andr.chiacchio@studenti.unina.it

(Corresponding author: Lorenzo Pagliara)



Fig. 1: Manual (left) vs teleoperated (right) dental procedures (pictorial views).

These procedures involve the preparation of the tooth, which entails the removal of hard tissue from the damaged or healthy tooth using rotary instruments mounted on dental handpieces [3]. Periodontal procedures include scaling and root planing (SRP), which involve the removal of plaque and calculus from the surfaces of the teeth and the smoothing of root surfaces, typically employing manual hand instruments and inserts mounted on sonic or ultrasonic handpieces [4]. Finally, although robotic computer-assisted implant surgery (r-CAIS) have shown a significant increase in the accuracy of dental implant placement [5], many operators still prefer the free-hand method for dental implantology [6].

Each of these procedures, even the simplest ones, require accuracy, extensively trained manual skills and dexterity.

Remark 1. *The oral cavity is a highly unstructured environment, which is full of natural obstacles that occlude the view of the surgical site and reduce the space for maneuvering, requiring constant changes in the orientation of the clinical tool and the operator's posture.*

Therefore, the successful outcome of a procedure, as well as the comfort for the patient, depend on both human factors, i.e., the experience and skills of the human operator [7], the adequacy of the instrumentation used and the duration of the treatments [8], and environmental factors [9], as highlighted in Remark 1. In particular, the latter factors can significantly affect the operator's comfort. In [10] a high prevalence of musculoskeletal disorders among dentists is reported. The main causes of these disorders can be traced back to an incorrect application of ergonomics, such as awkward pos-

tures, repetitive and prolonged movements, use of small or narrow tool handles, exertion of forces on hard or sharp objects, and exposure to vibrations [11]. Hence, when training new operators, much emphasis is placed on learning skills related to space utilization and positioning of surgical and non-surgical instruments, e.g., mirrors, to overcome occlusions, while maintaining healthy and comfortable posture [12]. In addition to this, to ensure the safety and effectiveness of the procedure, new operators must acquire skills related to the correct amount of pressure to apply to the site of interest, depending on the type of tool used.

Remark 2. *The sense of touch plays a key role in achieving successful and efficient procedures.*

This is also apparent from emerging trends in teaching, which make use of virtual environments and haptic devices (HD)s for training new operators [13], [14].

Robots can achieve accuracy, precision, efficiency beyond human capabilities. For this reason, the role of robots is to improve dental procedures, both in terms of patient satisfaction, i.e. broader access to care, reduced treatment time, fast recovery, and in terms of operator comfort, i.e., reduced workload intensity, increased visibility of the surgical field, improved ergonomics [15], as shown in Figure 1.

A. Related works

Haptic teleoperations are a technology that enables the remote execution of complex tasks, employing a robotic system.

Remark 3. *Haptic teleoperations combine the robot skills with the flexibility, dexterity, and cognitive capabilities of humans, while overcoming barriers in terms of distance, hazardous environments, and scales beyond human reach.*

By providing multiple types of sensory information, i.e. visual and haptic feedback, HBTs enable the human operator to experience *telepresence*, i.e. the perception of interacting with the remote environment as if it were directly encountered [16]. Furthermore, by integrating different haptic feedback and guidance modalities [17], [18], and shared control approaches [19], they contribute to reducing errors and enhance the efficiency, accuracy and safety of procedures, while also improving operator comfort and confidence. For these reasons, such technology is applied in multiple domains, such as telesurgery, space exploration, and the handling of hazardous materials in nuclear or underwater environments. However, in the context of dentistry, the adoption of such systems is still very limited.

The majority of research in robotics for dentistry is focused on oral implantology [20]. Robotic oral implant surgery offers significant benefits in terms of implant accuracy in partially [21] or totally edentulous patients, also compared to computer-assisted implant surgery (s-CAIS) systems [22]. Better placement accuracy, however, can be achieved at the expense of surgical efficiency, as shown in [23]. Such technologies also enable flapless dental implant placement, speeding up recovery time, reducing postoperative pain, and enhancing patient comfort [24]. [25] shows how a telerobotic-assisted drilling

system can enhance the accuracy of the human operator while preserving awareness of the procedure through an effective transmission of cutting forces and vibrations.

On the other hand, the state-of-the-art shows considerably less research effort in other free-hand procedures [26]. In the context of prosthetic procedures, robotics can enhance the precision of manual grinding using a turbine drill during tooth preparation [27] and can also compensate for hand tremors and the lack of tactile feedback in laser ablation [28], [29], improving accuracy [30] and efficiency [31]. In endodontics, robotics can automate and enhance precision and efficiency in root canal treatments [32], [33], outperforming current approaches also in effectively addressing biological and mechanical traits associated with biofilm recalcitrance and reinfection [34]. In periodontal procedures, robotic systems have the potential to increase accuracy, reducing the risk of errors and trauma to tissues by optimizing applied forces, as with other free-hand procedures. They can also improve the ergonomics for the operator, and comfort for the patient by speeding up recovery time. However, for such procedures, robotic technologies are still lacking [35], and there is no empirical evidence of such advantages.

Thus, although robotics shows promise in dental practice, several limitations remain. First, the quality of research is still insufficient in terms of clinical validation and technology readiness level (TRL) [36]. This is heavily influenced by the high costs of these robotic systems and the need to ensure their compatibility with existing clinical tools [37]. Second, the most widely used robots are fully autonomous, which require the development of state-of-the-art algorithms and advanced capabilities in perception, recognition, and exception handling [37]. In this context, the presence of a human is still necessary not only as a supervisor but also as an operator. In light of Remark 2 and Remark 3, and considering the impact on the operator acceptance [38], haptic teleoperations represent a viable solution. Moreover, the HBTs would allow the acquisition of human control strategies directly exercised in the robot state space, simplifying the process of transferring the knowledge from the human to the robot [39] and enabling the effective and objective evaluation of operator skills during training [40]. Finally, research tends to prioritize oral implantology over other dental procedures, despite the high number of daily free-hand routine procedures and the less invasiveness, entailing better patient acceptance [41]. Considering these limitations, [26] recommends to shift the focus from oral implantology procedures towards less invasive ones, which are better suited as forerunners in the field, and also to invest in educational robotics research in academia as a valuable tool to overcome the barrier of acceptance of robotic systems among future dentists.

B. Contributions

Motivated by the limitations or complete absence of robotic solutions for the most repetitive free-hand dental procedures, and in light of Remark 3, in this paper we present a HBTs for free-hand dental procedures (FH-HBTs), including:

- a dedicated mechanical end-effector, compatible with existing clinical tools and featuring an endoscopic camera, to improve visibility at the intervention site;
- a virtualized force feedback, consistent with the interaction observed through the visual feedback of the eye-in-hand camera, which enhances the haptic experience for the operator;
- a control system that ensures procedural safety, improves accuracy, and preserves manual dexterity, while providing motion correspondence between the operator's movements and those of the end-effector, as observed in the camera view.

To the best of the authors' knowledge, this is the only HBTS designed for free-hand dental procedures. Key contributions are:

- a control system to ensure accurate control of the tool center point (TCP) and to guarantee motion correspondence, using a novel eye-hand coordination strategy;
- a force limitation strategy that makes no previous assumption or estimation of the environment geometry, therefore accounting for the challenges outlined in Remark 1;
- eye-hand force correspondence provided with saturation and filtering via a deadband function;
- TRL-4 validation of the FH-HBTS on a free-hand procedure, consisting of dental scaling.

II. PRELIMINARIES

A. Notation

We denote by $\mathbf{T}_b^a \in SE(3)$ the homogeneous transformation matrix from frame a to frame b , in the form:

$$\mathbf{T}_b^a = \begin{pmatrix} \mathbf{R}_b^a & \mathbf{p}_b^a \\ \mathbf{0}^\top & 1 \end{pmatrix}, \quad (1)$$

where $\mathbf{R}_b^a \in SO(3)$ is the rotation matrix from frame a to frame b , and $\mathbf{p}_b^a \in \mathbb{R}^{3 \times 1}$ represents b 's origin in frame a .

We let \mathbf{x}_b^a be the pose of the frame b with respect to the frame a , corresponding to \mathbf{T}_b^a , in the form:

$$\mathbf{x}_b^a = \begin{bmatrix} \mathbf{p}_b^a \\ \mathbf{q}_b^a \end{bmatrix}, \quad (2)$$

where $\mathbf{q}_b^a \in \mathbb{H}_1$ is the quaternion associated with \mathbf{R}_b^a .

We denote by $\mathbf{R}_a^{\mathcal{F}}(\alpha) \in SO(3)$ the elementary rotation of an angle α about a generic axis \mathbf{a} of a frame \mathcal{F} .

We denote by $\mathbf{v}_b^a \in \mathbb{R}^{6 \times 1}$ the twist of the frame b with respect to the frame a , in the form:

$$\mathbf{v}_b^a = \begin{bmatrix} \dot{\mathbf{p}}_b^a \\ \dot{\boldsymbol{\omega}}_b^a \end{bmatrix}, \quad (3)$$

where $\dot{\mathbf{p}}_b^a, \dot{\boldsymbol{\omega}}_b^a$ are the linear and angular velocities, respectively.

B. Haptic device and robot reference frames

The frames used by the HD and the robot are reported in Figure 2. With regard to the HD, two frames are introduced:

- \mathcal{H}_b is the base reference frame, in which the HD's stylus poses and the feedback forces are expressed;
- \mathcal{H}_e is the HD's stylus frame.



Fig. 2: Haptic device and robot reference frames.

Regarding the robot, four frames are defined:

- \mathcal{R}_b is the base reference frame, in which motion references are expressed;
- \mathcal{R}_e is the robot's end-effector frame (computed from forward kinematics of joint measurements), corresponding to the TCP;
- \mathcal{R}_{ed} is the desired robot's end-effector frame, input to admittance control;
- \mathcal{R}_c is the compliant frame, output by the admittance control law.

We note that, after admittance control, motion control guarantees that \mathcal{R}_e tracks \mathcal{R}_c , as discussed next.

III. METHODOLOGY

The FH-HBTS we propose, shown in Figure 3, is based on a position-force architecture [42], coupling the leader (LR) and follower (FR) robots. The LR is an impedance HD, sensing the pose of the human operator and rendering haptic feedback according to the remote interaction between the FR and the environment. The HD is controlled by a leader controller, featuring an eye-hand coordination controller (EHCC) and a haptic feedback controller (HFC). The former is responsible for capturing the HD's stylus poses, filtering the human tremors, and generating the corresponding robot end-effector poses, so that the robot follows the stylus motion in coordination with the visual feedback. The latter is responsible for rendering the force feedback on the HD to let the human operator perceive the remote environment. Both controllers record data throughout the entire procedure. The FR is a position-controlled robot, instructed to track the HD through an admittance controller, which provides the latter with a configurable degree of compliance on its target pose with respect to the environment. Such controller has three key features. First, it ensures the stability of the FR, even in case of loss of communication, since, in case of a lack of reference from the EHCC, the controller keeps following the last one received. Second, it avoids damage to the arm structure and manipulated environment, since it adapts the received references to ensure compliant interaction with the surroundings. Finally, it limits the interaction forces by scaling the received motion references through a free-hand force limitation strategy embedded in the controller itself.

With reference to Figure 3, depicting the complete system, the following sections examine its individual subcomponents

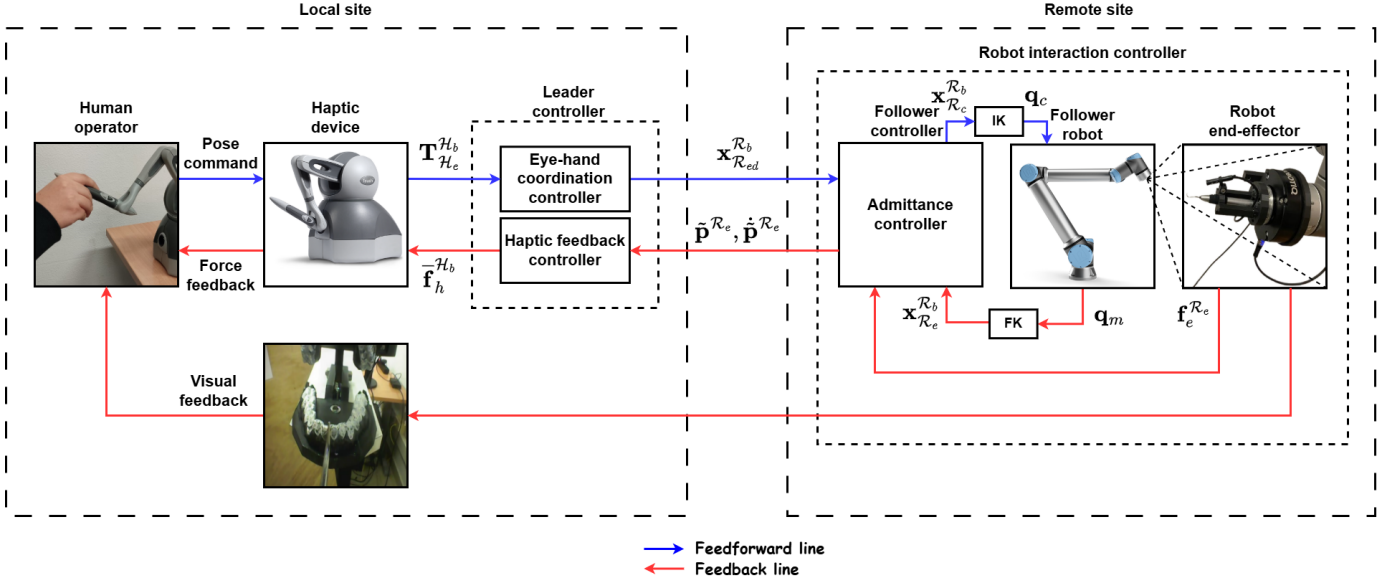


Fig. 3: Haptic bilateral teleoperation system scheme.

in detail. In Section III-A and Section III-C, a detailed description of the objectives and operation of the EHCC and HFC controllers is provided. In Section III-B the robot interaction control is described.

A. Eye-hand coordination controller

In a HBTS, visual feedback plays a crucial role in overcoming the limitations caused by distance. In teleoperated free-hand dental procedures, using an eye-in-hand camera is the most effective solution [43]. This approach enables the operator to maintain a consistently centered view of the operative field, offering a significant advantage over eye-to-hand camera configurations, where the view may be off-center with respect to the area of interest or obstructed by physical obstacles. In this context, the human operator is naturally guided by the video stream transmitted by the camera to provide commands to the FR via the HD. However, in the eye-in-hand configuration, a rotation of the tool (unavoidable, to preserve dexterity) causes a rotation of the viewing angle. This creates a mismatch between the movements expected by the operator and those actually executed by the robot in the camera view, compromising the accuracy of the task.

The da Vinci Surgical SystemTM, which requires the insertion of multiple tools to implement an eye-to-hand strategy, thereby increasing the bulk of the equipment and the overall costs, provides the motion correspondence between the operator's movements and those of the end-effector, observed in the camera view, by projecting the endoscope image above the surgeon's hands by means of mirrored overlay optics [44]. In our eye-hand coordination controller, we provide the motion correspondence at the command level, by creating a coupling between the HD's stylus and the robot's TCP, and appropriately converting the motion of the former into the motion of the FR. To enhance the naturalness of the teleoperation, a rotational coupling is also established between the HD's stylus and the FR's TCP. This includes defining the

desired relative rotation $\mathbf{R}_{\mathcal{H}_e}^{\mathcal{R}_e}$, and performing manually the alignment. This is done by the human operator during what we indicate as the *engagement phase*.

The latter is presented in Section III-A1, while the human tremors filtering and the eye-hand coordination mapping, implementing the motion correspondence, are discussed in Section III-A2 and Section III-A3, respectively.

1) *Engagement phase*: During the engagement phase, the EHCC retrieves the homogeneous transformation matrix of the HD's stylus $\mathbf{T}_{\mathcal{H}_e}^{\mathcal{H}_b}(k)$, and converts it into a robot's end-effector homogeneous transformation matrix with the following kinematic equations:

$$\mathbf{R}_{\mathcal{R}_{ed}}^{\mathcal{R}_b}(k) = \mathbf{R}_{\mathcal{H}_b}^{\mathcal{R}_b} \mathbf{R}_{\mathcal{H}_e}^{\mathcal{H}_b}(k) \left(\mathbf{R}_{\mathcal{H}_e}^{\mathcal{R}_e} \right)^\top, \quad (4)$$

$$\mathbf{p}_{\mathcal{R}_{ed}}^{\mathcal{R}_b}(k) = \mathbf{p}_{\mathcal{R}_e}^{\mathcal{R}_b}(k), \quad (5)$$

where $\mathbf{R}_{\mathcal{H}_b}^{\mathcal{R}_b}$ is the fixed rotation between \mathcal{H}_b and \mathcal{R}_b . We note that the position of the HD's stylus is not relevant for coupling, so it is converted to the current position of the robot's TCP. The obtained frame \mathcal{R}_{ed} is real-time displayed in a visualization tool, together with the actual robot end-effector one \mathcal{R}_e , as shown in Figure 4, so that the human operator, by acting on \mathcal{H}_e , can align the frame \mathcal{R}_{ed} with the frame \mathcal{R}_e . Once the alignment is accomplished, i.e. $\left[\mathbf{R}_{\mathcal{R}_{ed}}^{\mathcal{R}_b}(k) \right]^\top \mathbf{R}_{\mathcal{R}_e}^{\mathcal{R}_b}(k) = \mathbf{I}_3$, where $\mathbf{I}_3 \in SO(3)$ is the identity matrix, the engagement phase ends, i.e. HD and FR are aligned, and the human operator can begin teleoperation.

2) *Human tremors filtering*: At each control cycle, the EHCC retrieves the actual pose $\mathbf{x}_{\mathcal{H}_e}^{\mathcal{H}_b}(k)$ of the HD's stylus, corresponding to $\mathbf{T}_{\mathcal{H}_e}^{\mathcal{H}_b}(k)$. Exploiting such a pose to generate a command for the robot would result in transferring the human hand motion tremors, further accentuated by the control frequency. Therefore, $\mathbf{x}_{\mathcal{H}_e}^{\mathcal{H}_b}(k)$ is filtered online by a moving average filter for poses. At the k -th control cycle, the filtered

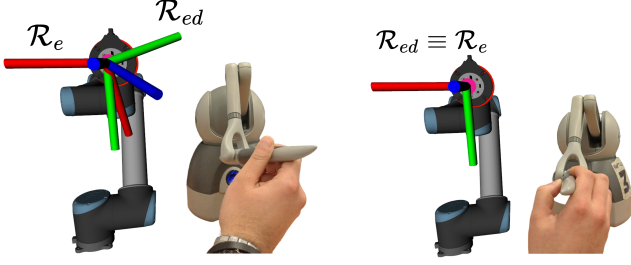


Fig. 4: Engagement phase supported by the visualization tool.

position $\bar{\mathbf{p}}_{\mathcal{H}_e}^{\mathcal{H}_b}(k)$ is obtained from the cumulative sum $\mathbf{s}(k)$ of samples within a window of fixed size n :

$$\bar{\mathbf{p}}_{\mathcal{H}_e}^{\mathcal{H}_b}(k) = \frac{\mathbf{s}(k)}{m} \quad (6)$$

where $m \leq n$ is the number of samples in the moving average window at the k -th control cycle, and the cumulative sum $\mathbf{s}(k)$ is:

$$\mathbf{s}(k) = \begin{cases} \mathbf{s}(k-1) + \mathbf{p}_{\mathcal{H}_e}^{\mathcal{H}_b}(k), & \text{if } k < n; \\ \mathbf{s}(k-1) + \mathbf{p}_{\mathcal{H}_e}^{\mathcal{H}_b}(k) - \mathbf{p}_{\mathcal{H}_e}^{\mathcal{H}_b}(k-n), & \text{otherwise.} \end{cases} \quad (7)$$

The filtered quaternion $\bar{\mathbf{q}}_{\mathcal{H}_e}^{\mathcal{H}_b}(k)$ is the eigenvector associated with the maximum eigenvalue of the $\mathbf{M}(k)$ matrix, of proper size [45], defined as:

$$\mathbf{M}(k) = \frac{\mathbf{c}(k)}{m}, \quad (8)$$

where $\mathbf{c}(k)$ is the cumulative sum of samples within a window of fixed size n , updated at each control cycle:

$$\mathbf{c}(k) = \begin{cases} \mathbf{c}(k-1) + \mathbf{q}_{\mathcal{H}_e}^{\mathcal{H}_b}(k) \left[\mathbf{q}_{\mathcal{H}_e}^{\mathcal{H}_b}(k) \right]^\top, & \text{if } k < n; \\ \mathbf{c}(k-1) + \mathbf{q}_{\mathcal{H}_e}^{\mathcal{H}_b}(k) \left[\mathbf{q}_{\mathcal{H}_e}^{\mathcal{H}_b}(k) \right]^\top + \\ - \mathbf{q}_{\mathcal{H}_e}^{\mathcal{H}_b}(k-n) \left[\mathbf{q}_{\mathcal{H}_e}^{\mathcal{H}_b}(k-n) \right]^\top, & \text{otherwise.} \end{cases} \quad (9)$$

Keeping the cumulative sums $\mathbf{s}(k)$ and $\mathbf{c}(k)$ enables achieving $\mathcal{O}(1)$ computational complexity.

3) *Eye-hand coordination*: In a HBTS, coupling two robots with different kinematics requires the use of mapping and scaling techniques. The literature shows that this coupling can be achieved by converting the motion of the HD into that of the FR through simple kinematic transformations, and appropriately scaling it to either expand the workspace size of the HD or enhance control accuracy [46]. In the eye-in-hand configuration, converting quantities between the two spaces without considering the viewing angle would lead to a loss of motion correspondence between the movements expected by the operator and those actually executed by the robot in the camera view. Therefore, in our EHCC, we transfer the HD's twist to the FR through an eye-hand coordination mapping and introduce dynamic scaling factors to improve control accuracy based on the task requirements.

Let $\Delta \bar{\mathbf{p}}_{\mathcal{H}_e}^{\mathcal{H}_b}(k)$ be the HD's displacement:

$$\Delta \bar{\mathbf{p}}_{\mathcal{H}_e}^{\mathcal{H}_b}(k) = \bar{\mathbf{p}}_{\mathcal{H}_e}^{\mathcal{H}_b}(k) - \bar{\mathbf{p}}_{\mathcal{H}_e}^{\mathcal{H}_b}(k-1), \quad (10)$$

and $\bar{\mathbf{R}}_{\mathcal{H}_e}^{\mathcal{H}_e}(k-1)$ the relative rotation:

$$\bar{\mathbf{R}}_{\mathcal{H}_e}^{\mathcal{H}_e}(k-1) = \begin{bmatrix} r_{11} & r_{12} & r_{13} \\ r_{21} & r_{22} & r_{23} \\ r_{31} & r_{32} & r_{33} \end{bmatrix}, \quad (11)$$

obtained from the quaternion $\bar{\mathbf{q}}_{\mathcal{H}_e}^{\mathcal{H}_e}(k-1)$:

$$\bar{\mathbf{q}}_{\mathcal{H}_e}^{\mathcal{H}_e}(k-1) = \left[\bar{\mathbf{q}}_{\mathcal{H}_e}^{\mathcal{H}_b}(k-1) \right]^\top \bar{\mathbf{q}}_{\mathcal{H}_e}^{\mathcal{H}_b}(k). \quad (12)$$

At each control cycle, the EHCC computes the HD's stylus twist:

$$\mathbf{v}_{\mathcal{H}_e}^{\mathcal{H}_b}(k) = \begin{bmatrix} \Delta \bar{\mathbf{p}}_{\mathcal{H}_e}^{\mathcal{H}_b}(k) \\ T_s \\ \vartheta \mathbf{r} \\ T_s \end{bmatrix}, \quad (13)$$

where T_s is the control period and \mathbf{r} and ϑ are the axis and the angle corresponding to $\bar{\mathbf{R}}_{\mathcal{H}_e}^{\mathcal{H}_e}(k-1)$, respectively:

$$\vartheta = \cos^{-1} \left(\frac{r_{11} + r_{22} + r_{33} - 1}{2} \right), \quad (14)$$

$$\mathbf{r} = \frac{1}{2 \sin \vartheta} \begin{bmatrix} r_{32} - r_{23} \\ r_{13} - r_{31} \\ r_{21} - r_{12} \end{bmatrix}. \quad (15)$$

From (13), the corresponding desired FR's end-effector twist is obtained as:

$$\mathbf{v}_{\mathcal{R}_{ed}}^{\mathcal{R}_e}(k) = \left[\mathbf{I}_2 \otimes \mathbf{R}_{\mathcal{R}_e}^{\mathcal{R}_b}(k) \right] \Lambda \left[\mathbf{I}_2 \otimes \mathbf{R}_{\mathcal{H}_e}^{\mathcal{R}_e}(k) \right] \cdot \left[\mathbf{I}_2 \otimes \mathbf{R}_{\mathcal{H}_e}^{\mathcal{H}_b}(k) \right]^\top \mathbf{v}_{\mathcal{H}_e}^{\mathcal{H}_b}(k). \quad (16)$$

where \otimes denotes the Kronecker product, Λ is the scaling diagonal matrix, of proper size, and $\mathbf{R}_{\mathcal{H}_e}^{\mathcal{R}_e}(k)$ is:

$$\mathbf{R}_{\mathcal{H}_e}^{\mathcal{R}_e}(k) = \mathbf{R}_{\mathcal{H}_e}^{\mathcal{R}_e} \mathbf{R}_{\mathcal{H}_e}^{\mathcal{H}_e}(\varphi(k)). \quad (17)$$

We note that $\mathbf{R}_{\mathcal{H}_e}^{\mathcal{R}_e}$ is the fixed rotation defining the mapping between quantities in \mathcal{H}_e and \mathcal{R}_e , and \mathbf{z} is the axis of \mathcal{H}_e mapped to the \mathbf{o} axis of \mathcal{R}_e , according to $\mathbf{R}_{\mathcal{H}_e}^{\mathcal{R}_e}$. The \mathbf{o} axis represents the optical axis of the camera in \mathcal{R}_e , which we assume to coincide with the \mathbf{z} axis of \mathcal{R}_e for negligible values of the camera tilt angle. Therefore, a rotation of $\varphi(k)$ about the \mathbf{z} axis of \mathcal{H}_e results in a viewing angle of $\varphi(k)$, as shown in Figure 5.

The rotation matrix $\mathbf{R}_{\mathcal{H}_e}^{\mathcal{H}_e}(\varphi(k))$ ensures the motion correspondence between the operator's movements and those of the FR's TCP in the camera view, by appropriately rotating the desired velocities according to the viewing angle. By setting $\mathbf{R}_{\mathcal{H}_e}^{\mathcal{H}_e}(\varphi(k)) = \mathbf{I}_3$ the mapping between twists becomes viewing angle independent:

$$\mathbf{R}_{\mathcal{H}_e}^{\mathcal{R}_e}(k) = \mathbf{R}_{\mathcal{H}_e}^{\mathcal{R}_e}, \forall k. \quad (18)$$

The desired FR's TCP homogeneous transformation $\mathbf{T}_{\mathcal{R}_{ed}}^{\mathcal{R}_b}(k)$ is obtained by numerically integrating the desired twist in (16). As for the desired rotation $\mathbf{R}_{\mathcal{R}_{ed}}^{\mathcal{R}_b}(k)$, it is obtained as:

$$\mathbf{R}_{\mathcal{R}_{ed}}^{\mathcal{R}_b}(k) = \mathbf{R}_{\mathcal{R}_e}^{\mathcal{R}_b}(k-1) \mathbf{R}_{\mathcal{R}_{ed}}^{\mathcal{R}_e}(k-1), \quad (19)$$

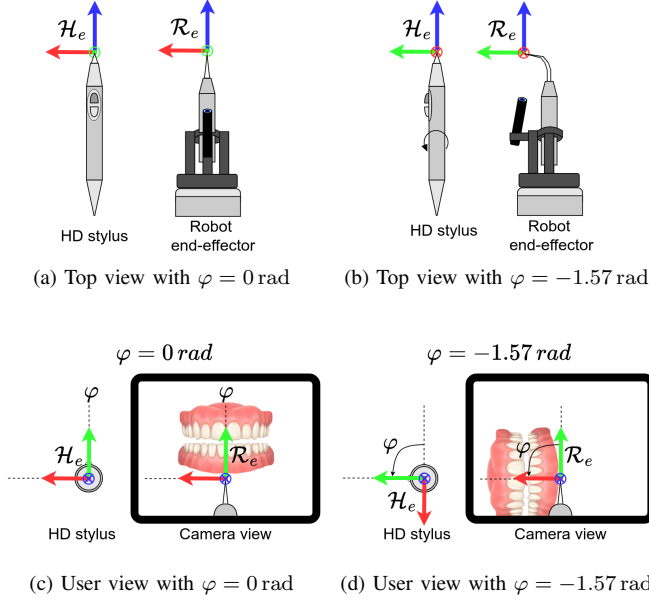


Fig. 5: Visualization of the rotational coupling between \mathcal{H}_e and \mathcal{R}_e .

where $\mathbf{R}_{\mathcal{R}_{ed}(k)}^{\mathcal{R}_e(k-1)}$ is the rotation matrix corresponding to the axis $\frac{\mathbf{r}}{\|\mathbf{r}\|}$ and angle ϑ :

$$\mathbf{r} = \left(\mathbf{R}_{\mathcal{R}_e}^{\mathcal{R}_b}(k-1) \right)^\top \boldsymbol{\omega}_{\mathcal{R}_{ed}}^{\mathcal{R}_b}(k) T_s, \quad (20)$$

$$\vartheta = \|\mathbf{r}\|. \quad (21)$$

As for the desired position $\mathbf{p}_{\mathcal{R}_{ed}}^{\mathcal{R}_b}(k)$, it is obtained as:

$$\mathbf{p}_{\mathcal{R}_{ed}}^{\mathcal{R}_b}(k) = \mathbf{p}_{\mathcal{R}_{ed}}^{\mathcal{R}_b}(k-1) + \dot{\mathbf{p}}_{\mathcal{R}_{ed}}^{\mathcal{R}_b}(k) T_s. \quad (22)$$

From $\mathbf{T}_{\mathcal{R}_{ed}}^{\mathcal{R}_b}(k)$ the desired FR's TCP pose is obtained as:

$$\mathbf{x}_{\mathcal{R}_{ed}}^{\mathcal{R}_b}(k) = \left[\mathbf{p}_{\mathcal{R}_{ed}}^{\mathcal{R}_b}(k)^\top \quad \mathbf{q}_{\mathcal{R}_{ed}}^{\mathcal{R}_b}(k)^\top \right]^\top. \quad (23)$$

The eye-hand coordination mapping and scaling can be turned into an algorithmic procedure with steps provided in Algorithm 1.

B. Robot interaction control

In this section, we first formalize the contact model between the robot and the environment (Section III-B1), and subsequently, we present the free-hand strategy for limiting the interaction forces (Section III-B2).

1) *Admittance model*: Let $\mathbf{x}_{\mathcal{R}_{ed}}^{\mathcal{R}_b}(k) = \left[\mathbf{p}_{\mathcal{R}_{ed}}^{\mathcal{R}_b}(k)^\top \quad \mathbf{q}_{\mathcal{R}_{ed}}^{\mathcal{R}_b}(k)^\top \right]^\top$ be the desired pose and \mathcal{R}_c the compliant frame specified by the quantities $\mathbf{p}_{\mathcal{R}_c}^{\mathcal{R}_e}(k)$, $\dot{\mathbf{p}}_{\mathcal{R}_c}^{\mathcal{R}_e}(k)$, $\ddot{\mathbf{p}}_{\mathcal{R}_c}^{\mathcal{R}_e}(k)$ and $\mathbf{q}_{\mathcal{R}_c}^{\mathcal{R}_e}(k)$. We do not consider compliance along the rotational axes, therefore, we assume $\mathbf{q}_{\mathcal{R}_c}^{\mathcal{R}_e}(k) = \mathbf{q}_{\mathcal{R}_{ed}}^{\mathcal{R}_e}(k)$. When the FR interacts with the environment, \mathcal{R}_c can be completely defined from $\mathbf{p}_{\mathcal{R}_{ed}}^{\mathcal{R}_e}(k)$, $\dot{\mathbf{p}}_{\mathcal{R}_{ed}}^{\mathcal{R}_e}(k)$ and $\ddot{\mathbf{p}}_{\mathcal{R}_{ed}}^{\mathcal{R}_e}(k)$, and the contact forces $\mathbf{f}^{\mathcal{R}_e}(k) \in \mathbb{R}^{3 \times 1}$, by integrating the mechanical impedance equation:

$$\mathbf{M}_d \ddot{\mathbf{p}}^{\mathcal{R}_e}(k) + \mathbf{K}_D \dot{\mathbf{p}}^{\mathcal{R}_e}(k) + \mathbf{K}_P \mathbf{p}^{\mathcal{R}_e}(k) = -\tilde{\mathbf{f}}^{\mathcal{R}_e}(k), \quad (24)$$

Algorithm 1 Eye-hand coordination mapping and scaling

Input: The HD's actual $\bar{\mathbf{x}}_{\mathcal{H}_e}^{\mathcal{H}_b}(k)$ and previous $\bar{\mathbf{x}}_{\mathcal{H}_e}^{\mathcal{H}_b}(k-1)$ filtered poses, and the previous desired pose $\mathbf{x}_{\mathcal{R}_{ed}}^{\mathcal{R}_b}(k-1)$

Output: The desired FR's TCP pose $\mathbf{x}_{\mathcal{R}_{ed}}^{\mathcal{R}_b}(k)$

- 1: Compute $\mathbf{v}_{\mathcal{H}_e}^{\mathcal{H}_b}(k)$ using (13)
- 2: Compute $\mathbf{v}_{\mathcal{R}_{ed}}^{\mathcal{R}_b}(k)$ using (16):
- 1) Convert $\mathbf{v}_{\mathcal{H}_e}^{\mathcal{H}_b}(k)$ into $\mathbf{v}_{\mathcal{R}_{ed}}^{\mathcal{R}_e}(k)$ and rotate it according to the viewing angle using (17):

$$\mathbf{v}_{\mathcal{R}_{ed}}^{\mathcal{R}_e}(k) := \left[\mathbf{I}_2 \otimes \mathbf{R}_{\mathcal{H}_e}^{\mathcal{R}_e}(k) \right] \left[\mathbf{I}_2 \otimes \mathbf{R}_{\mathcal{H}_e}^{\mathcal{H}_b}(k) \right]^\top \mathbf{v}_{\mathcal{H}_e}^{\mathcal{H}_b}(k)$$

- 2) Scale $\mathbf{v}_{\mathcal{R}_{ed}}^{\mathcal{R}_e}(k)$ using Λ and convert it into $\mathbf{v}_{\mathcal{R}_{ed}}^{\mathcal{R}_b}(k)$:

$$\mathbf{v}_{\mathcal{R}_{ed}}^{\mathcal{R}_b}(k) = \left[\mathbf{I}_2 \otimes \mathbf{R}_{\mathcal{R}_e}^{\mathcal{R}_b}(k) \right] \Lambda \mathbf{v}_{\mathcal{R}_{ed}}^{\mathcal{R}_e}(k)$$

- 3: Compute $\mathbf{T}_{\mathcal{R}_{ed}}^{\mathcal{R}_b}(k)$ from $\mathbf{v}_{\mathcal{R}_{ed}}^{\mathcal{R}_b}(k)$ using (19) and (22)
- 4: Extract $\mathbf{x}_{\mathcal{R}_{ed}}^{\mathcal{R}_b}(k)$ from $\mathbf{T}_{\mathcal{R}_{ed}}^{\mathcal{R}_b}(k)$

where $\mathbf{M}_d, \mathbf{K}_D, \mathbf{K}_P$ are the mass, damping, and stiffness diagonal matrices, respectively, of proper size, which are used to impose specific second-order mass-spring-damper dynamics; $\tilde{\mathbf{p}}^{\mathcal{R}_e}(k) = \mathbf{p}_{\mathcal{R}_{ed}}^{\mathcal{R}_e}(k) - \mathbf{p}_{\mathcal{R}_c}^{\mathcal{R}_e}(k)$ is the position error and $\dot{\tilde{\mathbf{p}}}^{\mathcal{R}_e}(k)$ and $\ddot{\tilde{\mathbf{p}}}^{\mathcal{R}_e}(k)$ its time derivatives; $\tilde{\mathbf{f}}^{\mathcal{R}_e}(k) = \mathbf{f}_d^{\mathcal{R}_e}(k) - \mathbf{f}_e^{\mathcal{R}_e}(k)$ is the force tracking error, defined as the difference between the desired force $\mathbf{f}_d^{\mathcal{R}_e}(k)$ and the exerted force $\mathbf{f}_e^{\mathcal{R}_e}(k)$, which is equal and opposite to the measured force. We take $\mathbf{f}_d^{\mathcal{R}_e}(k) = \mathbf{0}, \forall k \in \mathbb{N}_0$ to make the robot behave compliantly with the environment and $\dot{\tilde{\mathbf{p}}}^{\mathcal{R}_e}(k) = \ddot{\tilde{\mathbf{p}}}^{\mathcal{R}_e}(k) = \mathbf{0}, \forall k \in \mathbb{N}_0$ to reach a complete stop of the FR's end-effector upon reaching the target position, effectively preventing any collisions caused by further movement. From (24), the compliant position reference to be commanded to the robot is obtained as:

$$\mathbf{p}_{\mathcal{R}_c}^{\mathcal{R}_e}(k) = \mathbf{p}_{\mathcal{R}_{ed}}^{\mathcal{R}_e}(k) + \mathbf{R}_{\mathcal{R}_e}^{\mathcal{R}_c}(k) \mathbf{p}_{\mathcal{R}_{ed}}^{\mathcal{R}_e}(k). \quad (25)$$

2) *Free-hand force limitation strategy*: Assuming that the environment can be approximated by a linear spring model, the exerted force at the steady state [47] is:

$$\mathbf{f}_{ss}^{\mathcal{R}_e} = \mathbf{K}_{eq} \left(\mathbf{p}_{\mathcal{E}_r}^{\mathcal{R}_e} - \mathbf{p}_{\mathcal{R}_{ed}}^{\mathcal{R}_e} \right), \quad (26)$$

where $\mathbf{K}_{eq} = (\mathbf{K}_P \mathbf{K}_e)(\mathbf{K}_P + \mathbf{K}_e)^{-1}$ is the equivalent stiffness of the admittance stiffness \mathbf{K}_P and environmental stiffness \mathbf{K}_e [48], and $\mathbf{p}_{\mathcal{E}_r}^{\mathcal{R}_e}$ is the environment rest position. From (26), it follows that interaction forces can be limited through a suitable reference $\mathbf{p}_{\mathcal{R}_{ed}}^{\mathcal{R}_e}$ provided to the controller. Accurate limitation requires perfect knowledge of the environment that is particularly challenging to achieve, especially in a medical environment, in which the FR interacts with objects of varying stiffness and non-uniform geometry. Therefore, in the proposed strategy, the position reference:

$$\mathbf{p}_{\mathcal{R}_{ed}}^{\mathcal{R}_e}(k) = \left[\mathbf{R}_{\mathcal{R}_e}^{\mathcal{R}_b}(k) \right]^\top \mathbf{p}_{\mathcal{R}_{ed}}^{\mathcal{R}_b}(k) - \left[\mathbf{R}_{\mathcal{R}_e}^{\mathcal{R}_b}(k) \right]^\top \mathbf{p}_{\mathcal{R}_c}^{\mathcal{R}_b}(k), \quad (27)$$

is dynamically scaled based solely on the contact forces:

$$\mathbf{p}_{\mathcal{R}_{ed}}^{\mathcal{R}_e}(k) = \frac{1}{1 + K_s \left\| \mathbf{f}_e^{\mathcal{R}_e}(k) \right\|} \mathbf{p}_{\mathcal{R}_{ed}}^{\mathcal{R}_e}(k), \quad (28)$$

where $K_s \in \mathbb{R}^+$ is a proportional gain representing a trade-off between stability and responsiveness of the scaling action. Indeed, K_s close to 0 reduces sudden variations of $\mathbf{p}_{\mathcal{R}e}^{\mathcal{R}e}(k)$, even in presence of noisy force measures, but provides less force-limiting action. On the other hand, K_s significantly greater than 0 makes the scaling action more responsive, but may yield oscillations in the presence of noisy measurements. Therefore, to increase the system's robustness to noisy forces, exhibiting high-frequency variations, $\mathbf{f}_e^{\mathcal{R}e}$ is filtered online as done for positions in (6). We note that the strategy in (28) does not allow forces to be bounded below a predefined limit. However, it prevents contact forces from growing indefinitely, ensuring a limitation even in the transients of the interaction and for any orientation of the end-effector, without relying on the knowledge of the dental environment's complex geometry.

C. Haptic feedback controller

In performing medical procedures, the operator relies heavily on the sense of touch. Therefore, in a HBTS providing realistic haptic sensations, it becomes critical to the success of the procedures. In impedance systems, the interaction is captured by both the contact force $\mathbf{f}_e^{\mathcal{R}e}$ and the position error $\tilde{\mathbf{p}}^{\mathcal{R}e}$, the latter being characterized by slower transients than the former, which exhibits a step dynamics. As proposed in [49], replacing $\mathbf{f}_e^{\mathcal{R}e}$ with $\tilde{\mathbf{p}}^{\mathcal{R}e}$ to generate the force feedback makes each contact state transparent to the operator, preventing them from having to deal with sudden force changes they are not used to from previous training and fieldworks. Therefore, the proposed HFC defines a second (virtual) impedance model, generating the force feedback from the motion error of the admittance controller:

$$\mathbf{f}_h^{\mathcal{H}b}(k) = \mathbf{K}_h \tilde{\mathbf{p}}^{\mathcal{H}b}(k) + \mathbf{D}_h \dot{\tilde{\mathbf{p}}}^{\mathcal{H}b}(k), \quad (29)$$

where \mathbf{K}_h and \mathbf{D}_h respectively are virtual stiffness and damping diagonal matrices of the proper size. The position error $\tilde{\mathbf{p}}^{\mathcal{H}b}(k)$ and its time derivative $\dot{\tilde{\mathbf{p}}}^{\mathcal{H}b}(k)$ are defined, respectively, as:

$$\tilde{\mathbf{p}}^{\mathcal{H}b}(k) = \mathbf{R}_{\mathcal{H}e}^{\mathcal{H}b}(k) \left[\mathbf{R}_{\mathcal{H}e}^{\mathcal{R}e}(k) \right]^\top \tilde{\mathbf{p}}^{\mathcal{R}e}(k), \quad (30)$$

$$\dot{\tilde{\mathbf{p}}}^{\mathcal{H}b}(k) = \mathbf{R}_{\mathcal{H}e}^{\mathcal{H}b}(k) \left[\mathbf{R}_{\mathcal{H}e}^{\mathcal{R}e}(k) \right]^\top \dot{\tilde{\mathbf{p}}}^{\mathcal{R}e}(k). \quad (31)$$

We note that, as in (17), the rotation matrix $\mathbf{R}_{\mathbf{z}}^{\mathcal{H}e}(\varphi(k))$ is used to provide the force feedback correspondence with the interaction observed in the camera view. With regard to the \mathbf{K}_h and \mathbf{D}_h parameters of the virtual system in (29), they are tuned to provide a natural force feedback to the human operator while the FR interacts with the environment, decoupling it from the admittance control dynamics. Specifically, the stiffness matrix \mathbf{K}_h can be tuned to achieve the desired transient response, while the damping matrix \mathbf{D}_h can be tuned to mitigate vibrations. We envisage the possibility that the generated force feedback may exceed the range of forces that the HD device can exert. Therefore, the HFC saturates

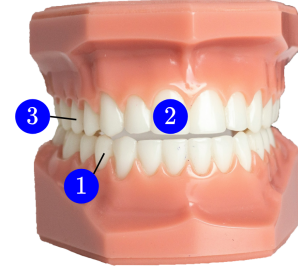


Fig. 6: Target teeth for dental scaling experiments: 1) lower right first premolar; 2) upper right central incisor; 3) upper right second premolar.

the norm of the force feedback $\|\mathbf{f}_h^{\mathcal{H}b}(k)\|$ to the maximum exertable force $f_{MAX}^{\mathcal{H}b} \in \mathbb{R}^+$:

$$\mathbf{f}_h^{\mathcal{H}b}(k) = \begin{cases} \mathbf{f}_h^{\mathcal{H}b}(k), & \text{if } \|\mathbf{f}_h^{\mathcal{H}b}(k)\| < f_{MAX}^{\mathcal{H}b}; \\ f_{MAX}^{\mathcal{H}b} \frac{\mathbf{f}_h^{\mathcal{H}b}(k)}{\|\mathbf{f}_h^{\mathcal{H}b}(k)\|}, & \text{otherwise.} \end{cases} \quad (32)$$

Finally, given the slow dynamics of $\tilde{\mathbf{p}}^{\mathcal{R}e}$, the human operator may perceive residual force feedback even when the robot is no longer interacting. To address this, we introduce a force dead-band $f_{db} \in \mathbb{R}^+$ to prevent the HD from reacting to such residuals:

$$\mathbf{f}_h^{\mathcal{H}b}(k) = \begin{cases} \mathbf{f}_h^{\mathcal{H}b}(k), & \text{if } \|\mathbf{f}_e^{\mathcal{R}e}(k)\| > f_{db}; \\ \mathbf{0}, & \text{otherwise.} \end{cases} \quad (33)$$

IV. EXPERIMENTAL VALIDATION

To evaluate the performance of the proposed FH-HBTS, we conduct interaction experiments using a phantom. Each experiment involves reaching a designated target tooth with an inactive dental scaler and applying a force to its surface, keeping the tool stationary. During the experiments, the robot remains out of the human operator's view, who relies solely on the visual feedback from the camera and the force feedback from the HD. We select three target teeth: the lower right first premolar, the upper right central incisor, and the upper right second premolar, as shown in Figure 6. The chosen targets are significant since each requires a different tool orientation, making the use of eye-hand coordination essential. For each target, we perform three interaction experiments with active force limitation and three without. With the aim of confirming the impact of the proposed strategy on the safety of interaction, we estimate, from the data recorded during the experiments, the conditional expectation of the interaction forces given a virtual penetration commanded by the operator. The conducted analysis is reported in Section IV-B.

In order to quantitatively assess the operation of the eye-hand coordination, we conduct a free-space experiment which concerns commanding the same spatial motion in the HD space, with different viewing angles. The results of the task execution are reported in Section IV-C.

Finally, we provide an experimental demonstration of the end-to-end system by conducting interaction experiments with

the three target teeth in both scenarios, this time emulating the dental scaling procedure. The outcomes of a dental scaling procedure execution, representative of the overall results are shown in Section IV-D.

A. Experimental setup

The experimental setup involves the following equipment and materials:

- a leader control station featuring a 6-degrees-of-freedom (DOF) force-feedback HD [50] and a workstation. The latter is a general purpose computer executing the leader controller loop, and communicating with the FR over an Ethernet network. In such a network, delays and packet losses are negligible, as is the case of an healthcare facility;
- a FR consisting of the 6-DOF UR10 robotic arm by Universal Robots [51]. It is equipped with an integrated mechanical end-effector for free-hand dental procedures. Its design is discussed in Section IV-A1;
- a dental phantom, i.e. 3D-printed life-sized model of a human mouth.

1) *Integrated mechanical end-effector*: In order to successfully perform any free-hand dental procedure, the operator relies on three basic factors: (a) the procedure-specific clinical tool; (b) the surgical field view, which may require external illumination and tools to show obstructed or poorly lit areas e.g., a mirror; (c) the sense of touch to ensure the right pressure to be exerted on the area of interest, in order to achieve a safe and effective procedure. In this work, we design an integrated mechanical end-effector, shown in Figure 7, that can provide all the tools and sensory capabilities required to perform free-hand dental procedures.

The designed end-effector consists of five main components:

- a *3D-printed mechanical interface* connecting the robot's flange with the force/torque sensor;
- a *force/torque sensor* measuring contact forces. The sensor used is the FT150 6-axis force/torque sensor by Robotiq [52];
- a *3D-printed tool socket* supporting the clinical tool and the endoscopic camera. The interface consists of a rigid structure to enable proper transmission of forces from the tool to the sensor, a circular hole, adjustable via a bolt-and-nut mechanism, to accommodate tools of different sizes, and a movable camera-support ring, allowing for adjustments of the view and light beam angle;
- an *HD endoscopic camera*, equipped with LED illumination to ensure good visibility even in poorly lit areas;
- a *clinical tool* for performing the procedure of interest. The tool is placed in the supporting socket after being wrapped with friction tape to ensure good mechanical compliance, emulating the skin friction between the operator's hand and the tool. The tool used for the chosen use case is a scaler.

2) Eye-hand coordination controller parametrization:

Given that the frequency of human hand tremors is around 6 Hz [53], we analyze the frequency response of a moving-average filter to identify the fixed window size n , such that

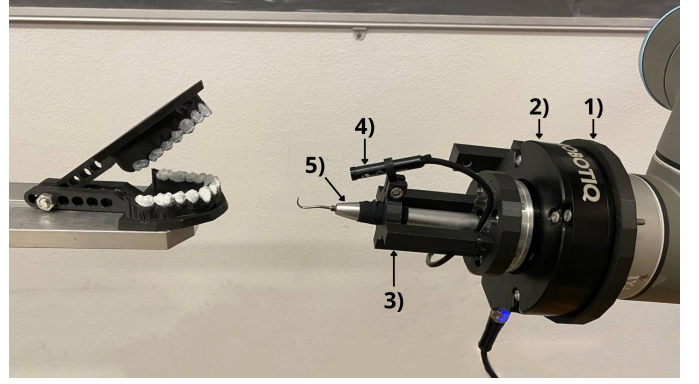


Fig. 7: Integrated mechanical end-effector for free-hand procedures, consisting of: 1) 3D-printed mechanical interface connecting the robot's flange with the force/torque sensor; 2) force/torque sensor; 3) 3D-printed tool socket supporting the clinical tool and the endoscopic camera; 4) HD endoscopic camera; 5) clinical tool. Visible in the left side of the figure is also the dental phantom used.

the cutoff frequency f_c is lower than that of the tremors. Based on the analysis conducted, we set $n = 50$, which guarantees a cutoff frequency $f_c \approx 2$ Hz.

With regard to the scaling factors, we set $\beta = 1$ and $\Lambda = \text{diag}(0.8, 0.8, 0.8, 1.0, 1.0, 1.0)$ to achieve high control accuracy on the translational axes without significantly reducing the workspace size.

3) *Admittance controller parametrization*: Since the interaction experiments require modest compliance and high damping along the normal axis, and greater and more precise positioning along the tangential axes, we set $\mathbf{K}_P = \text{diag}(50000, 50000, 6000)$, $\mathbf{K}_D = \text{diag}(2500, 2500, 12000)$ and $\mathbf{M}_d = \text{diag}(50, 50, 50)$.

Regarding the force limitation strategy, we identify a suitable trade-off between responsiveness and stability by setting $K_s = 0.06$, and by filtering the exerted forces with a moving average filter of window size $n = 500$.

4) *Virtual feedback parametrization*: With regard to the virtualization of the force feedback, the virtual impedance matrices are tuned to provide the human operator with a natural sensation, ensuring both smooth transient response and reduced vibrations. Therefore, we set $\mathbf{K}_h = \text{diag}(0.1, 0.1, 0.1)$, $\mathbf{D}_h = \text{diag}(0.5, 0.5, 0.5)$.

Regarding the force dead-band, we set $f_{db} = 1$ N.

B. Force limitation assessment

In order to assess the effectiveness of the proposed force limitation strategy, we perform 9 interaction experiments, with an average duration of approximately 20s each, 3 for each target tooth, with force limitation (Scenario A) and 9 more without force limitation (Scenario B). For each scenario we record the data sequence $\{a(k), b(k)\}_{1:N}$, sampling at a frequency of 125 Hz, where we set the component of the force normal to the surface $f_e^{\mathcal{R}_{e,\perp}}(k)$ as $a(k) \in \mathcal{A}$, and the virtual penetration commanded $\|\mathbf{p}_{\mathcal{R}_{ed}}^{\mathcal{R}_e}(k)\|$ as $b(k) \in \mathcal{B}$. From such data, we estimate the conditional probability function

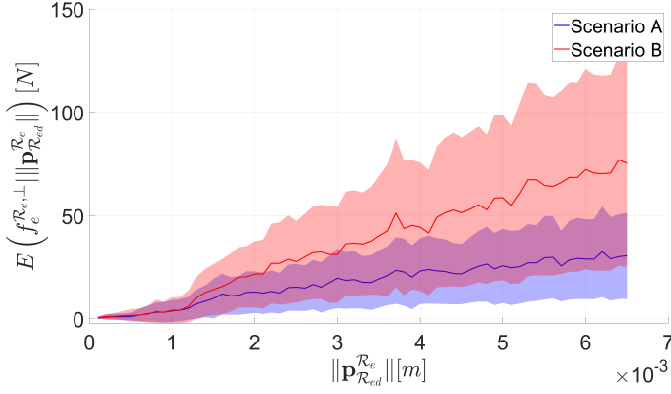


Fig. 8: Comparison between the conditional expectation of the interaction force in Scenario A and Scenario B.

$p(a(k)|b(k))$ using the histogram filter, as done in [54]. We discretize the set $\mathcal{A} = \{a \in \mathbb{R}^+ | a_{min} = 0 \text{ N} \leq a \leq a_{MAX} = 80 \text{ N}\}$ with a discretization step of $a_{step} = 0.1 \text{ N}$, and the set $\mathcal{B} = \{b \in \mathbb{R}^+ | b_{min} = 0 \text{ m} \leq b \leq b_{MAX} = 0.0065 \text{ m}\}$ with a discretization step of $b_{step} = 0.0001 \text{ m}$. The discretization steps a_{step} and b_{step} are selected based on the resolution of the force/torque sensor and the repeatability of the FR, respectively, while a_{MAX} and b_{MAX} are the maximum normal force and the maximum virtual penetration observed across all experiments. We obtain the empirical probability function $p(b(k))$ and the empirical joint probability function $p(a(k), b(k))$ by binning the data over the discretized sets, and estimate the conditional probability function $p(a(k)|b(k))$ by applying the Bayes rule.

Given the conditional probability function $p(a(k)|b(k))$, we estimate the conditional expectation $E(A|B)$, and the conditional variance $\text{Var}(A|B)$ following [55]. In Figure 8 are reported the conditional expectations of the exerted force $E(f_e^{R_e, \perp} || p_{R_{ed}}^{R_e})$ and the conditional standard deviation, obtained as the square root of the conditional variance $\text{Var}(f_e^{R_e, \perp} || p_{R_{ed}}^{R_e})$, in both scenarios. Visual inspection showcases a significant reduction in the expected normal interaction force in Scenario A, given the same virtual penetration commanded.

To evaluate the effectiveness of the force limitation strategy, we compare $E(f_e^{R_e, \perp} || p_{R_{ed}}^{R_e})$ and $\text{Var}(f_e^{R_e, \perp} || p_{R_{ed}}^{R_e})$ in both scenarios. To test whether the conditional variances differ significantly, we perform Levene's test and Bartlett's test. Levene's test shows that the conditional variances are significantly different (p -value $p \approx 0$), indicating that force limitation strategy affects the dispersion of normal force $f_e^{R_e, \perp}(k)$ with respect to virtual penetration $||p_{R_{ed}}^{R_e}(k)||$. Bartlett's test, which is more sensitive to normal distributions, confirms this observation ($p \approx 0$). This suggests that the difference in variance is not only due to the sampling effect but is a structural feature of the collected data. We compare the conditional expectation using a t-test for independent samples. Since Levene's test suggests a significant variance difference, we apply Welch's t-test, which is more robust in the case of unequal variances. The t-test returned a t-statistic value

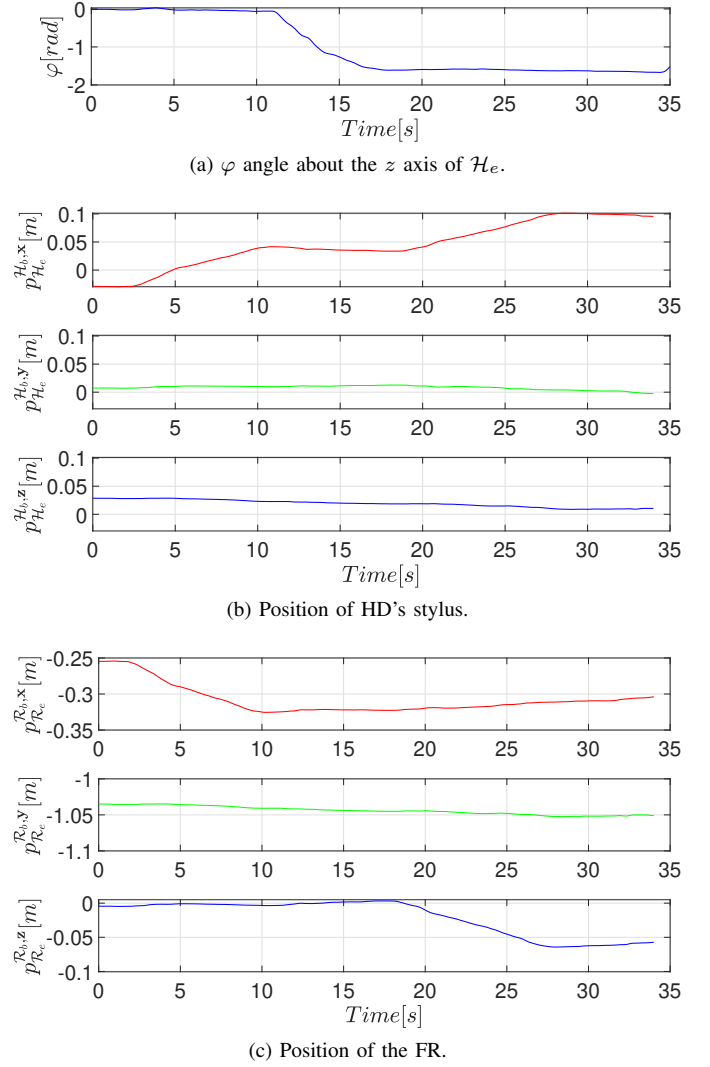


Fig. 9: Eye-hand coordination assessment.

of $t = -6.18$, confirming that the normal force is lower in Scenario A, and $p \approx 0$. Since such value is below the significance threshold $\alpha = 0.05$, we can reject the null hypothesis and conclude that the conditional expectations of normal force in the two scenarios are significantly different.

C. Eye-hand coordination assessment

In order to perform a formal assessment of eye-hand coordination, we execute a teleoperated task in the free space. The human operator performs a translatory motion with the HD, simultaneously rotating the viewing angle by rotating the HD's stylus by an angle φ about the z axis of \mathcal{H}_e . The validation is considered completed if the motion transferred to the robot varies as the viewing angle does. Figure 9 shows the φ angle, the position of HD's stylus and the position of the FR, respectively.

Results showcase that, as long as the angle $\varphi = 0 \text{ rad}$ (from 0 s to 10 s), a motion along the x axis of \mathcal{H}_b is mapped into a motion along the x axis of \mathcal{R}_b . When the angle turns into $\varphi = -\pi/2 \text{ rad}$, a motion along the x axis of \mathcal{H}_b is mapped into a motion along the z axis of \mathcal{R}_b (from 20 s to 30 s).

These results confirm that the mapping of motion between HD space and FR space is affected by the rotation of the visual field. However, they do not provide any suggestion regarding the effectiveness of eye-hand coordination for the human operator. Therefore, in the accompanying video¹ we provide a comprehensive qualitative assessment of the latter.

D. End-to-end system experimental demonstration

We provide a demonstration of the end-to-end system's operation in the accompanying video, where we showcase the execution of the dental scaling procedure on the three target teeth in Scenario A. In this section, we report the outcomes of the execution of a dental scaling procedure in Scenario A, highlighting two instants of the experiment (Figure 10), and compare them against those obtained in Scenario B (Figure 11). To avoid repetition, the analysis focuses on the outcomes of executing a dental scaling action on a single target tooth, the upper right second premolar.

In Figure 10d and Figure 11b, the normal forces exerted by the FR in both scenarios are shown. A visual inspection showcases a significant reduction in interaction forces when the free-hand force limitation strategy is active, with a decrease of approximately 50% in Scenario A, thereby confirming the validation presented in Section IV-B. The effectiveness of this strategy is made even more evident by comparing Figure 10c and Figure 11a. Notably, in Scenario A, where the interaction forces are lower, the virtual penetration commanded to the controller is even greater than in Scenario B. Nevertheless, as shown in Figure 10c, the implementation of this strategy enables the scaling of the provided references, effectively reducing the contact forces and enhancing the system's safety.

Finally, in Figure 10e and Figure 11c the forces rendered on the HD in both scenarios are shown. As expected, the results are consistent between the two scenarios, while both showing high similarity to exerted force profiles as well as slow dynamics. Such aspects enhance naturalness for the human operator.

V. DISCUSSIONS AND CONCLUSIONS

This paper proposed a FH-HBTS for free-hand dental procedures. The system features visual and haptic feedback, that are appropriately combined and coordinated to allow for a natural teleoperation experience. To improve the visibility of the intervention site, we designed a dedicated end-effector accommodating an eye-in-hand endoscopic camera, and ensuring compatibility with existing clinical tools. We also improved the accuracy of the procedure by introducing human tremor filtering and dynamic scaling of velocities. By providing the eye-hand coordination and the TCP control, we enabled the human operator to perceive the motion correspondence between their movements and those of the end-effector, observed in the camera view, preserving manual dexterity and expertise. Additionally, by appropriately transforming the virtualized

¹This paper has supplementary downloadable material available at <http://ieeexplore.ieee.org>, provided by the authors. This includes a multimedia MOV format movie clip, showing the end-to-end system experimental demonstration. This material is 51.4 MB in size.

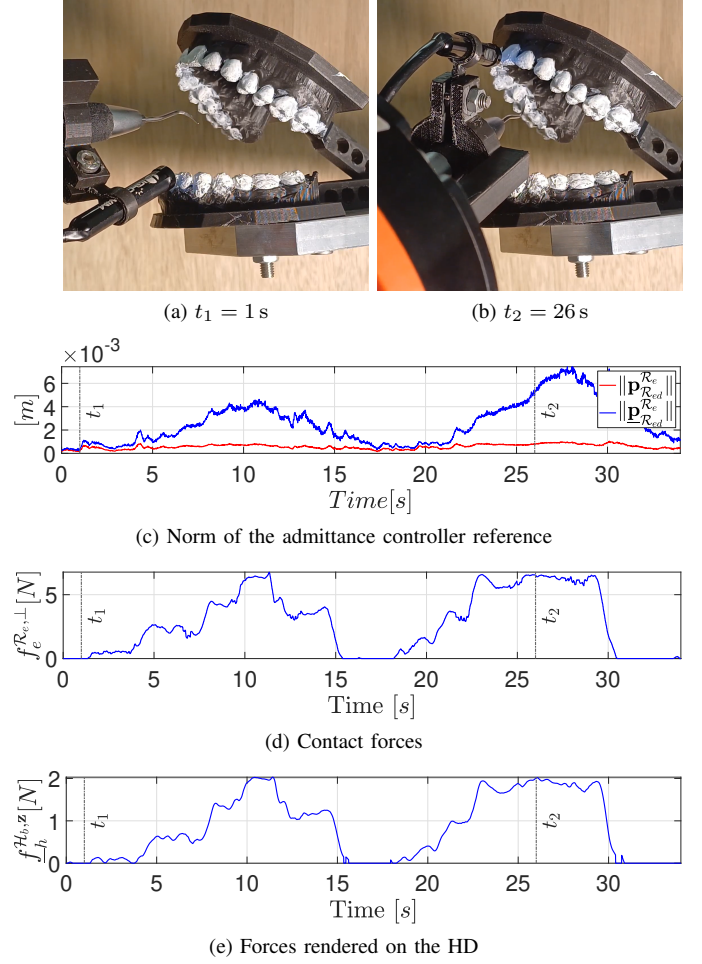


Fig. 10: Snapshots and outcomes of the dental scaling experiment in Scenario A.

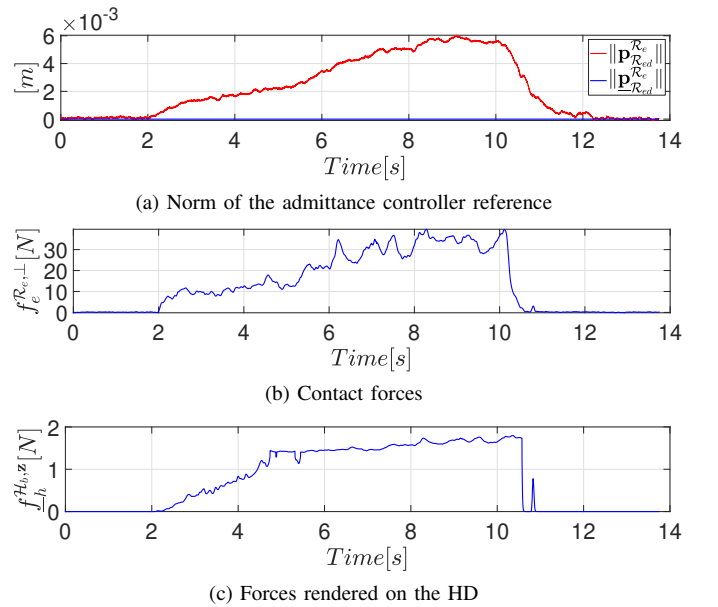


Fig. 11: Outcomes of the dental scaling experiment in Scenario B.

force feedback, we also ensured the force correspondence, enabling the human operator to experience a highly natural sensory perception. Finally, we enabled safe interactions, by scaling the motion references provided to the admittance controller. The proposed strategy allows for accurate force limitation in any contact state and for any orientation of the interaction tool, without requiring any prior modeling of the intervention site.

We believe that our FH-HBTS represents a crucial step towards a broader adoption of robotics in dentistry, as it allows for accurate treatments, while preserving the operator's cognitive and technical abilities. With respect to manual procedures, our system allows to preserve operator's ergonomics, track operator's performance, and enable remote healthcare.

We emphasize that the proposed system allows to collect haptic and motion data. While this feature is crucial during the training phase of new operators for the evaluation of learning metrics, i.e. learning curves [56], it is also central towards the deployment of data-driven control architectures that leverage demonstrations to synthesize control policies [57]. Finally, these data can also be used to learn cost functions [58], and hence intentions, of experts fulfilling a given task. In the context of dental procedures, this means that data collected from experts executing the procedure can be used to train policies for autonomous robots.

With our future work we plan to extend the FH-HBTS with autonomous patient motion compensation to further enhance the system's safety, and to benchmark the performance against the da Vinci Surgical SystemTM. Also, we plan to conduct experiments with professionals and active dental tools both to confirm the system usability under more representative clinical conditions and to collect expert policies for (semi-)autonomous procedures.

ACKNOWLEDGMENTS

The authors would like to thank Sabatino Panico for contributing to the system calibration and experimental campaigns.

REFERENCES

- [1] J. Grischke, L. Johannsmeier, L. Eich, L. Griga, and S. Haddadin, "Dentronics: Towards robotics and artificial intelligence in dentistry," *Dent. Mater.*, vol. 36, no. 6, pp. 765–778, Jun. 2020.
- [2] R. L. Quock, S. A. Patel, F. A. Falcao, and J. A. Barros, "Is a drill-less dental filling possible?" *Med. Hypotheses*, vol. 77, no. 3, pp. 315–317, Sep. 2011.
- [3] A. Podhorsky, P. Rehmann, and B. Wöstmann, "Tooth preparation for full-coverage restorations—a literature review," *Clin. Oral Invest.*, vol. 19, no. 5, pp. 959–968, Jun. 2015.
- [4] M. Sanz, D. Herrera, M. Kebschull, I. Chapple, S. Jepsen, T. Berglundh, A. Sculean, M. S. Tonetti, and EFP Workshop Participants and Methodological Consultants, "Treatment of stage i–III periodontitis—the EFP s3 level clinical practice guideline," *J. Clin. Periodontol.*, vol. 48, no. 1, pp. 4–60, Jan. 2021.
- [5] S. Yang, J. Chen, A. Li, K. Deng, P. Li, and S. Xu, "Accuracy of autonomous robotic surgery for single-tooth implant placement: A case series," *J. of Dent.*, vol. 132, p. 104451, May 2023.
- [6] A. Afshari, R. Shahmohammadi, S. A. Mosaddad, O. Pesteei, E. Hajmohammadi, M. Rahbar, M. Alam, and K. Abbasi, "Free-Hand versus Surgical Guide Implant Placement," *Adv. Mater. Sci. Eng.*, vol. 2022, no. 1, p. 6491134, Feb. 2022.
- [7] A. Kozlovsky, A. Rapaport, and Z. Artzi, "Influence of operator skill level on the clinical outcome of non-surgical periodontal treatment: a retrospective study," *Clin. Oral Invest.*, vol. 22, no. 8, pp. 2927–2932, Nov. 2018.
- [8] J. Y. N. Luo, P. P. Liu, and M. C. M. Wong, "Patients' satisfaction with dental care: a qualitative study to develop a satisfaction instrument," *BMC Oral Health*, vol. 18, no. 1, p. 15, Jan. 2018.
- [9] S. Schnutenhaus, M. Wagner, C. Edelmann, R. G. Luthardt, and H. Rudolph, "Factors Influencing the Accuracy of Freehand Implant Placement: A Prospective Clinical Study," *Dent. J.*, vol. 9, no. 5, p. 54, May 2021.
- [10] S. Y. Soo, W. S. Ang, C. H. Chong, I. M. Tew, and N. A. Yahya, "Occupational ergonomics and related musculoskeletal disorders among dentists: A systematic review," *Work*, vol. 74, no. 2, pp. 469–476, 2023.
- [11] A. Gupta, M. Bhat, T. Mohammed, N. Bansal, and G. Gupta, "Ergonomics in dentistry," *Int. J. Clin. Pediatr. Dent.*, vol. 7, no. 1, pp. 30–34, Apr. 2014.
- [12] J. Field, J. Dixon, A. Towers, R. Green, H. Albagami, G. Lambourn, J. Mallinson, W. Fokkinga, J. Tricio-Pesce, T. Crnić, and S. Vital, "Defining dental operative skills curricula: An ADEE consensus paper," *Eur. J. Dent. Educ.*, vol. 25, no. 2, pp. 405–414, May 2021.
- [13] E. L. McGleenon and S. Morison, "Preparing dental students for independent practice: a scoping review of methods and trends in undergraduate clinical skills teaching in the UK and Ireland," *Br. Dent. J.*, vol. 230, no. 1, pp. 39–45, Jan. 2021.
- [14] K. Uoshima, N. Akiba, and M. Nagasawa, "Technical skill training and assessment in dental education," *Jpn. Dent. Sci. Rev.*, vol. 57, pp. 160–163, Nov. 2021.
- [15] H. L. Abouzeid, S. Chaturvedi, K. M. Abdelaziz, F. A. Alzahrani, A. A. S. AlQarni, and N. M. Alqahtani, "Role of robotics and artificial intelligence in oral health and preventive dentistry - knowledge, perception and attitude of dentists," *Oral Health Prev. Dent.*, vol. 19, pp. 353–363, Jul. 2021.
- [16] G. Raju, G. Verghese, and T. Sheridan, "Design issues in 2-port network models of bilateral remote manipulation," in *Proc. Int. Conf. Robot. Autom.*, May 1989, pp. 1316–1321.
- [17] R. Yasin, P. Chalasani, N. Zevallos, M. Shahbazi, Z. Li, A. Deguet, P. Kazanzides, H. Choset, R. H. Taylor, and N. Simaan, "Evaluation of hybrid control and palpation assistance for situational awareness in telemanipulated task execution," *IEEE Trans. Med. Robot. Bionics*, vol. 3, no. 1, pp. 31–43, Feb. 2021.
- [18] D. Kundrat, A. Schoob, T. Piskun, R. Grässlin, P. J. Schuler, T. K. Hoffmann, L. A. Kahrs, and T. Ortmaier, "Toward assistive technologies for focus adjustment in teleoperated robotic non-contact laser surgery," *IEEE Trans. Med. Robot. Bionics*, vol. 1, no. 3, pp. 145–157, Aug. 2019.
- [19] Z. Deng, X. Wei, C. Pan, G. Li, and Y. Hu, "Shared control of tendon-driven continuum robots using visibility-guaranteed optimization for endoscopic surgery," *IEEE Trans. Med. Robot. Bionics*, vol. 6, no. 2, pp. 487–497, May 2024.
- [20] A. Y. Alqutaibi, H. H. Hamadallah, B. Abu zaid, A. M. Aloufi, and R. A. Tarawah, "Applications of robots in implant dentistry: A scoping review," *J. Prosthet. Dent.*, Dec. 2023.
- [21] Y. Wu, S. Zou, P. Lv, and X. Wang, "Accuracy of an autonomous dental implant robotic system in dental implant surgery," *J. Prosthet. Dent.*, vol. 133, no. 3, pp. 764–770, Aug. 2024.
- [22] S. Xi, J. Hu, G. Yue, and S. Wang, "Accuracy of an autonomous dental implant robotic system in placing tilted implants for edentulous arches," *J. Prosthet. Dent.*, Sep. 2024.
- [23] Z. Xu, Y. Xiao, L. Zhou, Y. Lin, E. Su, J. Chen, and D. Wu, "Accuracy and efficiency of robotic dental implant surgery with different human-robot interactions: An in vitro study," *J. Dent.*, vol. 137, p. 104642, Oct. 2023.
- [24] H. S. Talib, G. N. Wilkins, and I. Turkylmaz, "Flapless dental implant placement using a recently developed haptic robotic system," *Br. J. Oral Maxillofac. Surg.*, vol. 60, no. 9, pp. 1273–1275, Nov. 2022.
- [25] Y. Kasahara, H. Kawana, S. Usuda, and K. Ohnishi, "Telerobotic-assisted bone-drilling system using bilateral control with feed operation scaling and cutting force scaling," *Int. J. Med. Robot. Comput. Assisted Surg.*, vol. 8, no. 2, pp. 221–229, Jun. 2012.
- [26] P. Ahmad, M. K. Alam, A. Aldajani, A. Alahmari, A. Alanazi, M. Stoddart, and M. G. Sghaireen, "Dental robotics: A disruptive technology," *Sensors*, vol. 21, no. 10, p. 3308, Jan. 2021.
- [27] J. Jiang, Y. Guo, Z. Huang, Y. Zhang, D. Wu, and Y. Liu, "Adjacent surface trajectory planning of robot-assisted tooth preparation based on augmented reality," *Eng. Sci. Technol. Int. J.*, vol. 27, p. 101001, Mar. 2022.

- [28] L. Wang, D. Wang, L. Ma, Y. Zhang, F. Yuan, Y. Sun, and P. Lv, "Preliminary experiments of a miniature robotic system for tooth ablation using ultra-short pulsed lasers," in *Proc. IEEE/RSJ Int. Conf. Intell. Robots Syst.*, 2013, pp. 2566–2571.
- [29] L. Wang, D. Wang, Y. Zhang, L. Ma, Y. Sun, and P. Lv, "An automatic robotic system for three-dimensional tooth crown preparation using a picosecond laser," *Lasers Surg. Med.*, vol. 46, no. 7, pp. 573–581, 2014.
- [30] L. Ma, Y. Zhang, D. Wang, P. Lv, Y. Sun, and H. Wang, "Trajectory tracking control of a miniature laser manipulation robotic end-effector for dental preparation," in *Proc. IEEE Int. Conf. Robot. Biomim.*, Dec. 2013, pp. 468–473.
- [31] F. Yuan and P. Lyu, "A preliminary study on a tooth preparation robot," *Adv. Appl. Ceram.*, vol. 119, no. 5, pp. 332–337, 2020.
- [32] J. Dong and H. Everett, "The development of endodontic micro robot," in *Proc. ASME Int. Mech. Congr. Expo.*, May 2009, pp. 201–204.
- [33] J. Dong and S. Y. Hong, "Design of z axis actuator and quick tool change assembly for an endodontic micro robot," in *Proc. ASME Int. Mech. Eng. Congr. Expo.*, 2012, pp. 507–511.
- [34] G. Hwang, A. J. Paula, E. E. Hunter, Y. Liu, A. Baber, B. Karabucak, K. Stebe, V. Kumar, E. Steager, and H. Koo, "Catalytic antimicrobial robots for biofilm eradication," *Sci. Rob.*, vol. 4, no. 29, 2019.
- [35] L. Liu, M. Watanabe, and T. Ichikawa, "Robotics in dentistry: A narrative review," *Dent. J.*, vol. 11, no. 3, p. 62, Feb. 2023.
- [36] T. C. T. van Riet, K. T. H. Chin Jen Sem, J.-P. T. F. Ho, R. Spijker, J. Kober, and J. de Lange, "Robot technology in dentistry, part two of a systematic review: an overview of initiatives," *Dent. Mater.*, vol. 37, no. 8, pp. 1227–1236, 2021.
- [37] Z. Xia, F. Ahmad, H. Deng, L. Jiang, W. Qin, Q. Zhao, and J. Xiong, "Robotics application in dentistry: A review," *IEEE Trans. Med. Rob. Bionics*, vol. 6, no. 3, pp. 851–867, 2024.
- [38] Y. Li, Y. Inamochi, Z. Wang, and K. Fueki, "Clinical application of robots in dentistry: A scoping review," *J. Prosthodont. Res.*, vol. 68, no. 2, pp. 193–205, 2023.
- [39] H. Ravichandar, A. S. Polydoros, S. Chernova, and A. Billard, "Recent advances in robot learning from demonstration," *Annu. Rev. Control Robot. Auton. Syst.*, vol. 3, no. 1, pp. 297–330, 2020.
- [40] M. Li, Y.-H. Liu, and Q. Huang, "An optimized haptic interaction model based on support vector regression for evaluation of endodontic shaping skill," in *Proc. IEEE Int. Conf. Robot. Biomim.*, 2007, pp. 617–622.
- [41] M. N. Milner, E. C. Anania, K. Candelaria-Oquendo, S. Rice, S. R. Winter, and N. K. Ragbir, "Patient perceptions of new robotic technologies in clinical restorative dentistry," *J. Med. Syst.*, vol. 44, no. 2, 2019.
- [42] G. Niemeyer, C. Preusche, S. Stramigioli, and D. Lee, "Telerobotics," in *Springer Handb. Robot.*, 2016, pp. 1085–1108.
- [43] G. Flandin, F. Chaumette, and E. Marchand, "Eye-in-hand/eye-to-hand cooperation for visual servoing," in *Proc. IEEE Int. Conf. Robot. Autom.*, Apr. 2000, pp. 2741–2746.
- [44] C. Freschi, V. Ferrari, F. Melfi, M. Ferrari, F. Mosca, and A. Cuschieri, "Technical review of the da vinci surgical telemanipulator," *Int. J. Med. Robot. Comput. Assisted Surg.*, vol. 9, no. 4, pp. 396–406, 2013.
- [45] F. L. Markley, Y. Cheng, J. L. Crassidis, and Y. Oshman, "Averaging Quaternions," *J. Guid. Control Dyn.*, vol. 30, pp. 1193–1197, Jul. 2007.
- [46] M. Radi, "Workspace Scaling and Haptic Feedback for Industrial Telepresence and Automation Systems with Heavy-duty Teleoperators," in *Forschungsberichte IWB*, 2012.
- [47] H. Gao, X. Zhang, C. Ma, and C. Zhou, "Combined active and passive adaptive variable admittance compliant control for space robotic manipulators," in *Proc. IEEE Int. Conf. Robot. Biomimetics*, 2023.
- [48] Z. Li, H. Huang, X. Song, W. Xu, and B. Li, "A fuzzy adaptive admittance controller for force tracking in an uncertain contact environment," *IET Control Theory Appl.*, vol. 15, no. 17, pp. 2158–2170, Nov. 2021.
- [49] L. Pagliara, E. Ferrentino, A. Chiacchio, and G. Russo, "Safe haptic teleoperations of admittance controlled robots with virtualization of the force feedback," in *Proc. IEEE Int. Conf. Autom. Sci. Eng.*, Aug. 2024, pp. 1574–1579.
- [50] 3D Systems, "Touch - Haptic Device," <https://www.3dsystems.com/haptics-devices/touch>, 2016.
- [51] Universal Robots, "Collaborative robotic automation — universal robots cobots," <https://www.universal-robots.com/>, 2024.
- [52] Robotiq, "Robotiq," <https://robotiq.com>, 2024.
- [53] S. Calzetti, M. Baratti, M. Gresty, and L. Findley, "Frequency/amplitude characteristics of postural tremor of the hands in a population of patients with bilateral essential tremor: implications for the classification and mechanism of essential tremor," *J. Neurol. Neurosurg. Psychiatry*, vol. 50, no. 5, pp. 561–567, 1987.
- [54] E. Garrabè and G. Russo, "Probabilistic design of optimal sequential decision-making algorithms in learning and control," *Annu. Rev. Control*, vol. 54, pp. 81–102, Jan. 2022.
- [55] R. Steyer and W. Nagel, *Probability and Conditional Expectation: Fundamentals for the Empirical Sciences*. John Wiley & Sons, 2017.
- [56] M. Zhuang, J. Chen, B. Tao, M. Gul, F. Wang, and Y. Wu, "Exploring the learning curve of dental implant placement using a task-autonomous robotic system among young dentists from different specialties—a pilot module study," *Clin. Implant Dent. Relat. Res.*, 2024.
- [57] D. Gagliardi and G. Russo, "On a probabilistic approach to synthesize control policies from example datasets," *Autom.*, vol. 137, p. 110121, 2022.
- [58] E. Garrabè, H. Jesawada, C. D. Vecchio, and G. Russo, "On convex data-driven inverse optimal control for nonlinear, non-stationary and stochastic systems," *Autom.*, vol. 173, p. 112015, 2025.



Lorenzo Pagliara (Student Member, IEEE) received the M.Sc. degree in Computer Engineering with honors from University of Salerno, Fisciano, Italy, in 2021. He is currently a Ph.D. candidate in Information Engineering at University of Salerno. His research interests cover haptic teleoperations, interaction control human–robot collaboration, and medical robotics.



Enrico Ferrentino (Member, IEEE) received his M.Sc. degree in Computer and Automation Engineering from the Polytechnic University of Turin, Italy, and his Ph.D. degree in Robotics from the University of Salerno, Italy. From 2013 to 2014, he was a Visiting Scholar at NASA's Jet Propulsion Laboratory in Pasadena, USA, where he contributed to the Axel tethered robot project within the Robotic Mobility group, led by Dr. I. Nesnas. Between 2014 and 2017, he served as a Ground Segment Engineer at ALTEC S.p.A., Turin, Italy, working on the ESA robotic mission ExoMars. In 2019, he was a Visiting Scholar at LAAS-CNRS in Toulouse, France, where he participated in the H2020 PRO-ACT project as part of the team led by Prof. A. Franchi. Since 2020, he has been a Lecturer in Robotics and Medical Robotics with the Department of Information and Electric Engineering and Applied Mathematics at the University of Salerno, where he currently serves as an Assistant Professor and technical advisor of the Robotics Laboratory, led by Prof. P. Chiacchio. In 2024, he was appointed Associate Editor of the IEEE Transactions on Automation Science and Engineering. His research interests include optimal planning and control of robotic manipulators, force control, haptic teleoperations, human-robot collaboration, and software architectures for robot control, with applications spanning industrial, medical, and aerospace robotics.



Andrea Chiacchio He graduated with honors with a Master's degree in Odontoiatria e protesi dentaria from the Università Cattolica del Sacro Cuore - Roma. He is currently enrolled in the residency program in Oral Surgery at the University of Naples Federico II and collaborates with the Department of Medicine, Surgery and Dentistry at the University of Salerno. With a strong interest in innovation in the dental field, he is dedicated to research in robot-assisted medicine, exploring the potential of these advanced technologies to enhance surgical practices

and patient treatment.



Giovanni Russo (Senior Member, IEEE) is an Associate Professor of Automatic Control at the University of Salerno, Italy. He was previously with the University of Naples Federico II (Ph.D. in 2010), Italy, Ansaldo STS (System Engineer/Integrator of the Honolulu Rail Transit Project, USA in 2012–2015), IBM Research Ireland (Research Staff Member in Optimization, Control and Decision Science from 2015 to 2018) and University College Dublin, Ireland (in 2018–2020). His research interests include contraction theory, analysis/control

of nonlinear and complex systems, neuro-inspired decision-making under uncertainty and control in the space of densities. Dr. Russo has served as Associate Editor for the IEEE Transactions on Circuits and Systems I: regular papers (2016–2019) and the IEEE Transactions on Control of Network Systems (2017–2023). Since January 2024, Dr. Russo is serving as Senior Editor for the IEEE Transactions on Control of Network Systems.